Analysis of the Frequency Dependence of LIGO Directional Sensitivity (Antenna Pattern) and Implications for Detector Calibration

Hunter Elliott[1]
Mentors: Rick Savage[2]**, Greg Mendell**[2]
and Malik Rakhmanov[3]

Abstract

The current LIGO calibration technique's application is limited to the primary frequency band from DC to 8 kHz. It assumes a constant antenna pattern and approximates the detector's length response, resulting in a systematic, frequency dependent error. The recent addition of two high-frequency bands centered on the cavity free spectral range frequency of 37.52 kHz and its first integer multiple 75.04kHz requires that the calibration be modified. The effect of the gravitational-wave frequency on the antenna pattern is discussed and quantified. The frequency dependence of the detectors length response is analyzed with emphasis on the gravitational-wave frequencies corresponding to multiples of the cavity free spectral range. A modified calibration procedure is proposed that eliminates the systematic error in addition to allowing calibration in the high-frequency band.

[1] The Colorado College, Colorado Springs, CO, USA. Contact: h_elliott@coloradocollege.edu
[2] LIGO Hanford Observatory, PO Box 159, Richland, WA 99352, USA
[3] Department of Physics, University of Florida, Gainseville, FL 32611, USA

Introduction

Interferometric gravitational wave observatories such as LIGO have sensitivities that are dependent on source location, frequency and polarization. The interpretation of any signal from the observatory must take these dependences into account. Currently the angular dependence (source location and polarization) is separated from the source frequency dependence for purposes of calibration. This simplifies and streamlines the calibration and software injection process. However the separation utilizes two approximations, which limit the bandwidth of its application. The detector is sensitive to high frequency gravitational waves and several high frequency sources have been proposed yet calibration and injection at high frequencies, where these approximations breakdown, is impossible with the current technique. The approximations are not essential, merely convenient, and it is therefore possible to modify the procedure to allow calibration and injection at all frequencies. Furthermore these changes can be integrated seamlessly into the current calibration and injection methods without inconveniencing those involved.

Length Response

LIGO intends to detect gravitational waves through the length variations they produce in the detector arms. Whether caused by gravitational waves or not, the response of the detector to length changes of different frequencies must be considered for an accurate calibration.

Altering the position of one of the interferometer's end test masses will produce a signal 4km away at the interferometer dark port. This deviation from resonance propagates from the end test mass to the beam splitter at the speed of light. For deviations with a frequency below the cavity pole ($f < f_{cav} = 1/\tau \approx 90Hz$ where τ is the storage time) the test mass' positions are essentially communicated instantaneously. Therefore in this band the frequency of oscillation is unimportant and the magnitude of the response is determined solely by the amplitude of the perturbation. As the frequency of these length changes increases the finite propagation time for light in the cavity becomes significant and the response of the interferometer's signal to length changes falls off approximately as $1/f$. However as the period of the perturbations becomes of order of the transit time for a photon in the arms, T, this $1/f$ falloff ends and the response begins to climb towards its DC value again. To understand why consider the length fluctuations from the point of view of an individual photon in the arms. Assume that the length is being driven at a frequency

$$f = \frac{cn}{2L} \equiv \frac{n}{2T} \quad n = 0,1,2,3\ldots \tag{1}$$

where c is the speed of light, L the length of the interferometer arms and for this example $n > 0$. Furthermore assume that this photon reflects off the end test mass just as it is passing through the midpoint of its oscillations. The photon then traverses the arm, reflects off the input test mass and returns once again to the end test mass. This trip took

exactly 2T, which at these frequencies is an integer multiple of the period of the end test mass oscillations. Therefore when the photon again encounters the end test mass it has returned to the midpoint of its oscillations and from the point of view of the photon the cavity length is static. The length response at these frequencies should therefore be the same as at DC. We would then expect a length response that peaks where (1) is satisfied and falls off approximately as $1/f$ away from these peaks. This is in fact a good description of the length response and its analytical form is shown in Figure 1[1]:

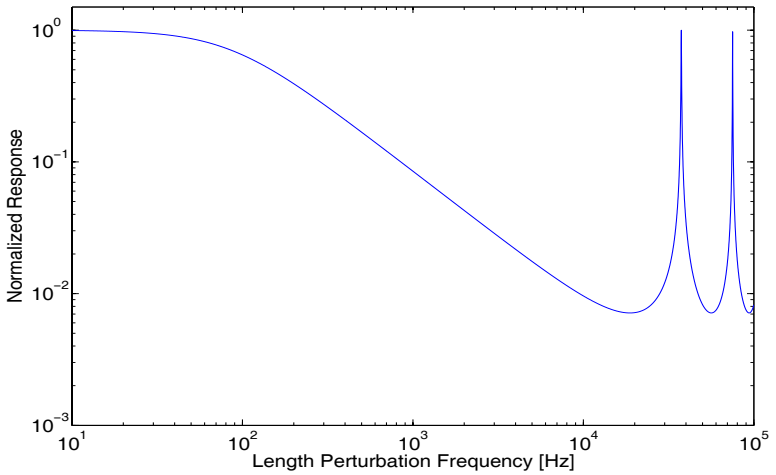

Figure 1 – Normalized detector length response.

There is a relatively flat area from DC to the cavity pole at 90Hz followed by a long $1/f$ falloff. Where (1) is satisfied, which also corresponds to multiples of the cavity free spectral range (FSR), the response returns to its DC value. It is important to note here that despite their appearance when plotted logarithmically, the higher order peaks at $f=nf_{FSR}$, $n=1,2,3\ldots$ are all of the same shape and have the same 90Hz half-width as the DC peak. See Appendix B for a linearly scaled plot and a more thorough treatment of the length response.

Of course everything stated about length response applies to the detection of a gravitational wave via the length changes it produces. Therefore if a search for gravitational waves is to be conducted it would be done most efficiently in the vicinity of one of the peaks in the length response. The primary LIGO band does exactly this, straddling the peak at $n=0$ from DC to 8kHz. Recent proposals to use the higher order peaks[2] have resulted in the addition of two high frequency bands centered around the n = 1 and n = 2 peaks at 37.52 kHz and 75.04 kHz respectively. However this presents a problem for the calibration of the instrument. Established before the addition of these high-frequency bands, the current calibration approximates the length response and therefore lacks features in this response that lie outside the primary band (Figure 2):

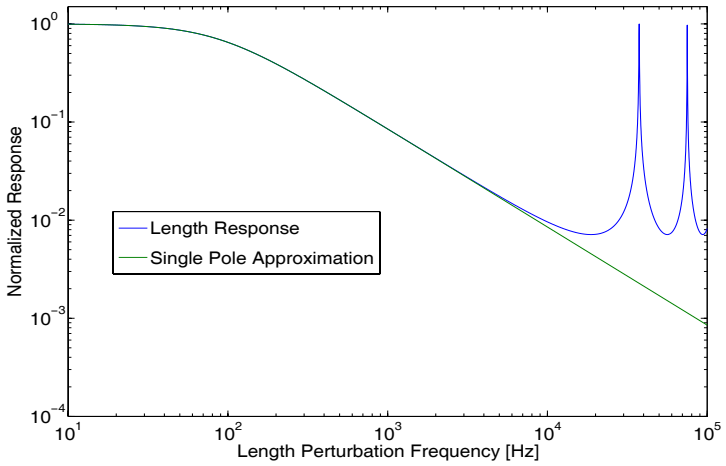

Figure 2 – Comparison of full length response and the single pole approximation currently in use.

This comparison reveals two facts about the current approximation: First that it is valid within the primary band, with an error of less than 8% at 8kHz. Second it shows that it is *not* valid at higher frequencies; the increased response in the vicinity of these recently added channels is *not* accounted for. The full analytical length response must therefore be used if calibration, injection and data collection are to occur at these higher frequencies (See the Appendix C for more on calibration and injection). This modification will of course have the added benefit of removing the small systematic error in the current calibration, and will in fact be in place in time for analysis of the S4 data[3].

Gravitational Wave Response

With the response to length changes out of the way we can now discuss the response to the gravitational waves (GWs) that produce those length changes. This is more complicated because two gravitational waves of the same magnitude and frequency but incident from different directions will produce different length changes in the interferometer. For example a GW incident in-line with one arm will not produce a response in said arm because the waves are transverse but the other arm will experience strain. If the same GW were incident from directly above the detector, perpendicular to its plane, both arms would see strain and the response would be double that seen in the former case. Additionally if a GW is incident from a non-orthogonal angle each arm will see only the projection of the GW onto its axis and therefore measure less than the full strain. This directional dependence is visualized through antenna patterns:

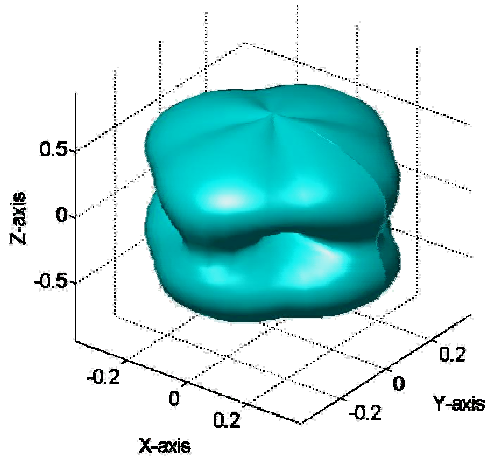

Figure 3 – Antenna pattern at f_{gw}= 0 Hz for all polarizations. Patterns for plus and cross polarization components and an explanation of what that means can be found in Appendix A.

In these plots the distance from the origin to the surface of the pattern in a particular direction gives the relative sensitivity in that direction. The beam splitter would lie at the origin, the X-Arm along the positive x-axis and the Y-Arm along the y-axis.

If Figure 3 represented the entirety of the detector's directional dependence then the combination of it and the detector length response would give the overall sensitivity. In fact for long-wavelength GWs this is essentially true. If one assumes that the period of the gravitational wave is much greater than T the antenna pattern is independent of frequency and Figure 1and Figure 3 completely describe the detectors sensitivity; the directional dependence handled by the antenna pattern geometry and the frequency dependence by the length response. One could picture this as an antenna pattern of the shape given in Figure 3 but scaled at each frequency by the length response given in Figure 1. However in actuality the antenna pattern geometry is *not* independent of frequency; not only should the antenna patterns change size with frequency due to the length response, but their shape should alter also. To understand why these patterns depend on GW frequency you must consider how the strain is altering during the time a photon is traversing the arms. At low frequencies the transit time is much shorter than the GW period and can be approximated as T = 0. This is referred to as the long wavelength approximation and results in a frequency-independent antenna pattern geometry. This approximation is currently used in the primary band. However at higher frequencies, where the period of the gravitational wave is of order T, the strain is varying significantly during the time the photon travels from one mirror to the other and T can no longer be approximated as zero. When this is true the direction of the photons propagation becomes important; if it is traveling generally in the same direction as the gravitational wave their relative velocity is small (< c) and the photon will sample only a small portion of the GW's phase. If the photon is traveling in generally the opposite direction as the GW then their relative velocity is large (> c) and the photon will sample a much larger portion of the GW's phase. This discrepancy between the forward and return trips results in a frequency-dependent antenna pattern geometry.

This leaves us with two frequency dependencies; that of the length response and that of the antenna pattern geometry. The second frequency dependence is visualized in Figure 4:

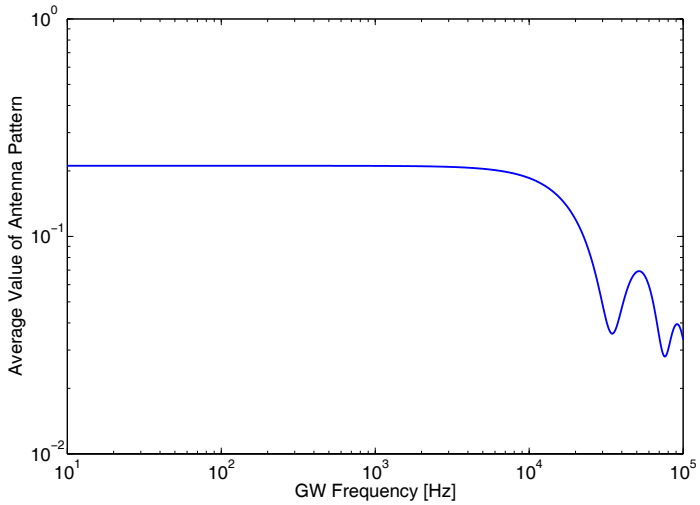

Figure 4 – Frequency dependence of the antenna pattern geometry.

This dependence is relatively flat over the primary LIGO band, justifying the use of the long wavelength approximation there (See Appendix A for a more thorough justification). However at high frequencies, particularly in the vicinity of the first FSR frequency, the average value of the pattern is approximately a factor of five smaller than at DC. Plotting the antenna pattern geometry at the first FSR reveals that this is not simply a change in scale; the shape is quite different (Figure 5).

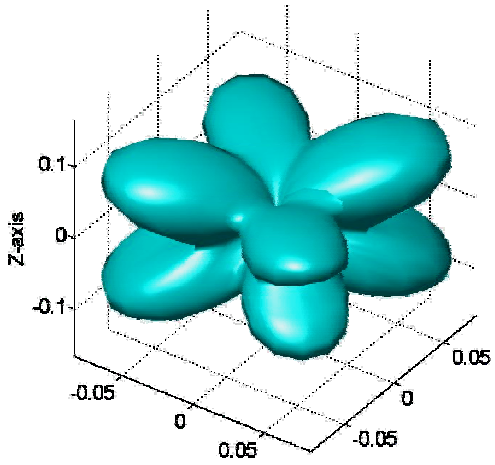

Figure 5 – Antenna pattern for at $f_{gw} = f_{1FSR}$ = 37.52 kHz for all polarizations.

The long wavelength approximation and the static antenna pattern geometry that results from it are therefore not valid for data collection or injection in the two high frequency channels. One way to fix this problem would be to assume that the pattern geometry in Figure 5 applied to the entire 1FSR high frequency channel and similarly that the pattern geometry in the second high frequency channel was the same as at 2FSR. This is analogous to the low frequency assumption of a static antenna pattern and would give comparable accuracy (See Appendix A). However there is another option that would not be subject to the systematic errors associated with assuming a constant antenna pattern. That is to simply use the correct antenna pattern at each frequency. The practical problem

with this is that real-world sources have a finite bandwidth, meaning the antenna pattern geometry would be different for each frequency component of the source. This is significantly more involved than using a single pattern for all frequencies. To avoid this burden a Matlab® function E.m was written. It accepts a time-series of strain, scales each frequency component of that signal using the correct antenna pattern and then returns the properly scaled time series. For more on this function see Appendix D and for more on the antenna pattern geometry frequency dependence see Appendix A.

Figure 4 has one more significant consequence; the dip in average pattern geometry size near f_{FSR} means that though the length response is the same there as it is at DC the overall sensitivity of the detector will be lower by a factor of approximately 5.

Overall Sensitivity

To determine the frequency dependence of the overall detector sensitivity one must combine the antenna pattern geometry and the length response. Giving full, three dimensional antenna patterns *with* frequency dependence would require 4 dimensions and is not easily displayed on paper. This problem can be avoided by using the average over all angles of the antenna pattern geometry, as plotted in Figure 4. Combining this with the length response (Figure 2) gives us a plot of the overall sensitivity:

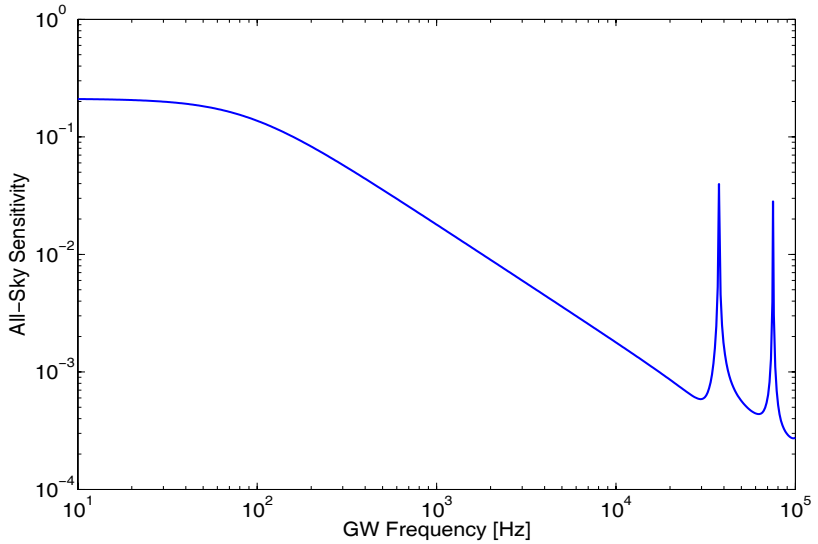

Figure 6 – All-Sky averaged detector sensitivity versus frequency.

This shows that although the length response at multiples of the FSR is the same as at DC the overall sensitivity is not. This is a result of the decreased antenna pattern geometry size (Figure 4) near the FSR frequencies.

Conclusions

Using LIGO to search for high-frequency gravitational waves in addition to the primary low frequency search is an exciting, relatively new idea. Potential sources in these high frequency channels include the stochastic background[4], high-order neutron star vibrational modes and high-frequency components of black hole ring down predicted by

string theory[5]. However the calibration and injection procedures currently in place will not suffice at these high frequencies. The modifications required to extend the calibration and injection to the new high-frequency channels are minor and can be implemented without inconvenience to LIGO staff.

Appendix A - Directional Dependence

The detector's directional dependence or antenna pattern is described in a coordinate system determined by the detector *and by the gravitational wave source location*:

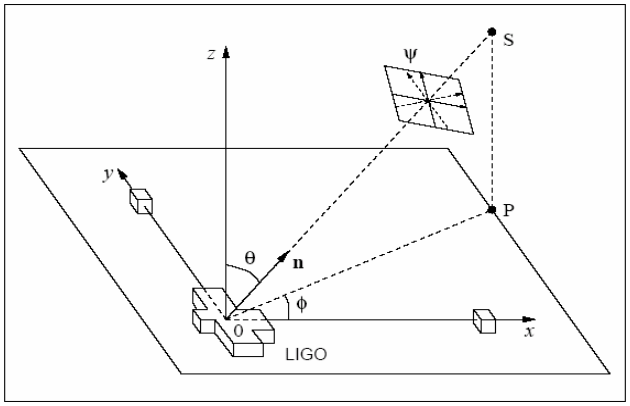

Figure 7 - Coordinate system for source location description[6].

The detector's X-arm lies along the x-axis and the Y-arm along the y-axis with the beam splitter at the origin. Throughout this paper source sky locations will be referred to using ϕ and θ as defined in Figure 7. The source orientation angle ψ is defined relative to the 'line of nodes.' This is the line that describes the intersection of the plane that is perpendicular to the gravitational waves propagation and the plane of the detector. The angle between this line of nodes and the x-axis of the wave frame is ψ. It is important to note that this results in a dynamic orientation angle; what is defined by $\psi = 0$ varies depending on the source location and in fact is undefined at $\theta = 0$ or π, where the two planes that define the line of nodes are parallel. In these special circumstances ψ is defined as the angle between the detector frame x-axis and the wave frame x axis.

To get a general sense of such a detector's antenna pattern let us first consider a gravitational wave incident at ϕ, θ and $\psi = 0$. Note that this is a situation in which there is no line of nodes and so the detector's x-axis takes its place. This source location is often referred to as 'optimally-oriented'. In this scenario one arm is stretching while the other is contracting i.e. the strain components in the X and Y-arm directions are 180^o out of phase. This is therefore a prime sky location (ϕ, θ) for detecting gravitational waves and we would expect the antenna pattern to have a large value for this direction and it's 'opposing' sky location, at $\theta = 180^o$ and $\varphi = 0^o$. Because gravitational waves are transverse, plus-polarized sources incident in-line with the X-arm ($\theta=90^o$, $\phi=0^o$) will only be seen in the Y-arm and vice-versa. This tells us that the net effect for GWs incident along either arm will be half of that seen with the 'optimally-oriented' source and the antenna pattern should reflect this. Finally let's look at sources incident along the line that bisects the two arms in the plane of the detector ($\theta=90^o$, $\phi=45^o$). This will induce strain in both arms to the same degree and in-phase. The two cancel, the net effect is zero, and our antenna pattern should have a value of zero for this direction. Rather than reasoning through each individual source angle one can derive an expression for the Pound-Drever-Hall signal produced by a gravitational wave of a particular frequency,

polarization and sky location. This function has been derived previously[6,7,8] and evaluating it for various sky locations gives a three-dimensional antenna pattern:

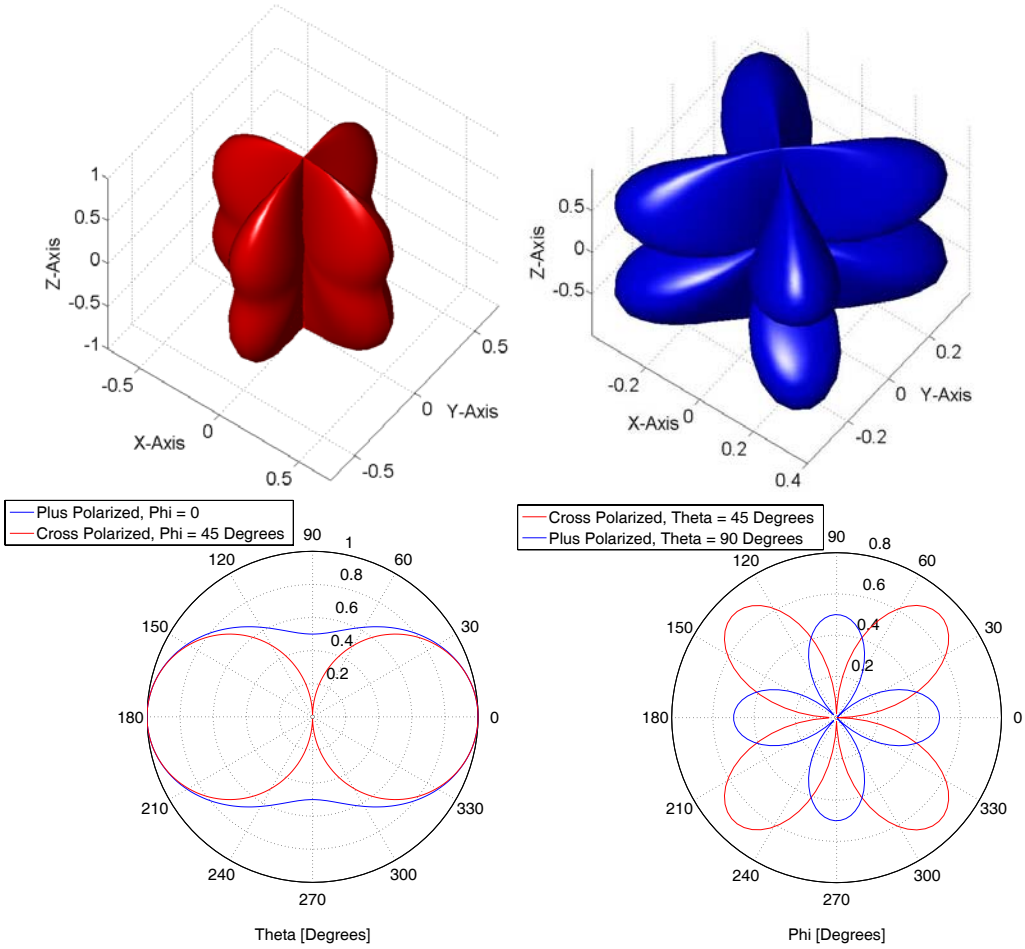

Figure 8 - Top: Full Antenna pattern at DC for plus (red) and cross (blue) polarized gravitational waves. Bottom Left: Cross-section of antenna patterns at a constant φ given by legend. Bottom Right: Cross-section of antenna pattern at a constant θ given by legend.

When displayed in this manner (Figure 8) the distance from the origin to the surface in any direction is proportional to the detector's sensitivity in that direction. The patterns are also normalized so that the highest sensitivity is represented by a distance from the origin of 1. This means that for example the antenna pattern of a detector that was equally sensitive in all directions would be a unit sphere.

These three-dimensional plots are helpful in spatially relating the sensitivity to the actual detector. However they are not conducive to the determination of the precise angle corresponding to any particular peak or valley in the antenna pattern. For this purpose the antenna patterns can be plotted as two-dimensional 'carpet' diagrams (Figure 9):

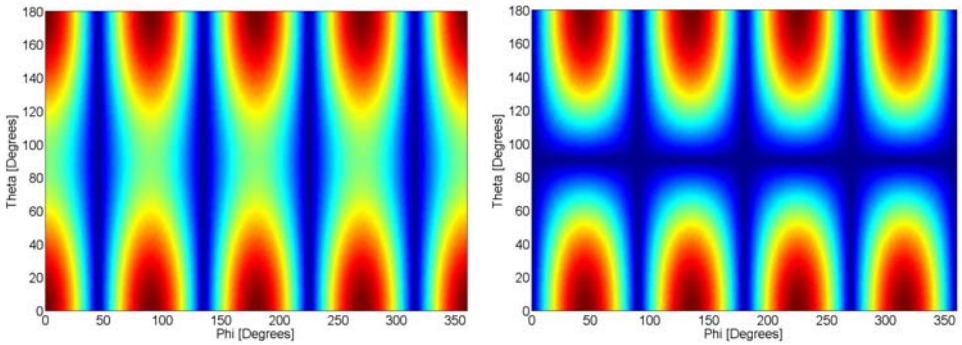

Figure 9– Carpet Antenna patterns at DC for plus (left) and cross (right) polarizations. Color indicates sensitivity with red being highest and blue lowest.

Color is now used in place of radius to indicate sensitivity. The darkest shade of red corresponds to a normalized sensitivity of one and the darkest blue to a sensitivity of zero. Plotting the information this way allows the φ and θ corresponding to any particular lobe on the three dimensional patterns to be easily determined.

In general the arguments made so far about the directional sensitivity of the detector have not considered the frequency of the incident gravitational wave. This would be justified if the strain of the gravitational wave were measured by both of the interferometer's arms instantaneously. Then only the geometry of the detector and the transverse nature of gravitational radiation would need to be considered. In reality the strain is being sampled by photons traversing the arms, traveling from the input test mass to the end test mass in T = 13.326μs. When the period of the gravitational wave is much greater than T the strain effectively *is* measured instantaneously and the geometry of the antenna pattern is therefore essentially static. Another way to phrase this is that for long-period GWs the strain can be considered constant over any single photon round-trip. These assumptions result in an antenna pattern that is independent of frequency, which allows the DC patterns to be used throughout the primary LIGO band as is currently the practice. However as frequency increases and f_{gw}^{-1} becomes of order T the GWs phase, and therefore the experienced strain, can no longer be considered static over a photon round-trip. A photon traveling in the direction of the GW's propagation will still see approximately the same phase of the GW throughout its trip. However on its return trip, when it is traveling against the GW, it will see a much wider range of phase. This discrepancy between the forward and return trips results in directional sensitivity that cannot be deduced simply from the geometry of the situation, as was true at DC.

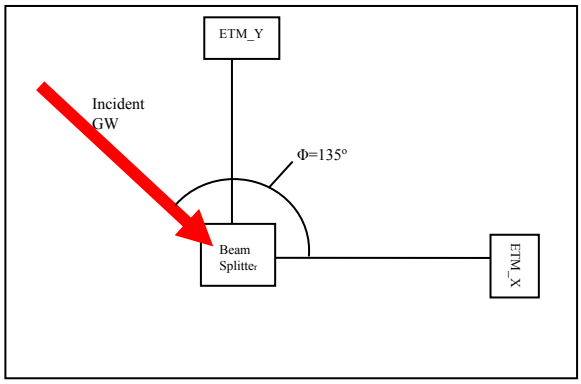

Figure 10 – Overhead view of detector showing GW incident at θ =90°, φ=135 °

For example consider a plus-polarized GW incident from θ = 90° and φ = 135° as depicted in Figure 10. Similar to the source bisecting the arms, at DC this scenario results in both arms seeing equal strain components and therefore producing no response. Now let's look at the same source location but with $f_{gw} = \frac{c}{2L} \equiv \frac{1}{2T}$ where L is the length of the detector arms and c is the speed of light in vacuum. This frequency is unique in that the period of the GW is identical to 2T, the round trip time of a photon in one of the arms. It and its integer multiples are of importance and will be discussed in detail later. First consider a photon traveling from the beam splitter to ETM_Y. This photon is traveling generally in the opposite direction as the GW and their relative velocity is ~2c. Therefore the photon will see approximately one full wavelength of the GW and because of cancellation the net effect will be small. On the return trip the photon will be traveling with the GW and therefore see essentially the same GW phase for the entire trip; cancellation is not possible, the strain is high for the entire trip and the effect is large. Closely examining Figure 10 we see that for the X-arm the situation is reversed. That is the X-arm forward trip is identical to the Y-arm return trip and vice versa. This means that primary contribution to the photons' phase alteration will be in the return trip for the Y-arm and the forward trip in the X-arm. Because the return trip starts T seconds after the forward trip and $f_{gw}^{-1} = 2T$ the strain seen in both of the return trips is out of phase relative to that seen in the forward trips. Therefore the only significant contributions, which come from the Y-arm return trip and the X-arm forward trip, are in opposing directions and the net effect is double that seen in either arm. This is in stark contrast to the DC case, where the net effect was zero and viewing a plot of the antenna pattern for this frequency (Figure 11) confirms that it is very different from that at DC.

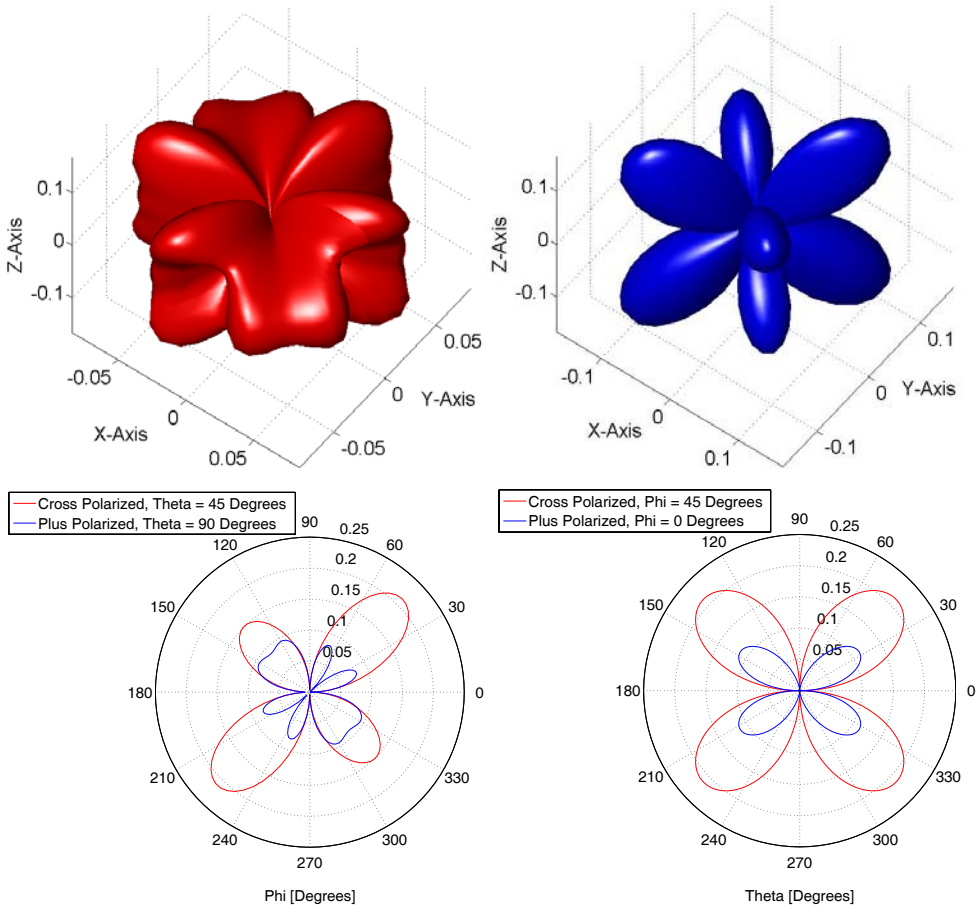

Figure 11– Top: Antenna patterns for plus (red) and cross (blue) polarized gravitational waves at 1FSR. Bottom: Cross-sections of antenna patterns at constant angles given by the legends.

The same cancellation that prevented the Y-arm forward trip and the X-arm return trip in the previous example (Figure 10) from affecting the overall detector response can also cause nulls in the antenna pattern. Let's again consider a GW incident along the x-arm of the detector but this time of a frequency $f_{gw}^{-1} = 2T$ as in the last example. Because the wave is transverse the X-arm will still not be affected. The Y-arm, as before, will experience strain but this time cancellation plays a role. For the forward trip the photon sees one half of the GW's phase, and on the return trip it sees the second half. The two trips cancel and the net effect is zero. These phenomena thoroughly complicate the detector's directional dependence.

Plotting the average value of the antenna pattern versus frequency (Figure 12) gives us an idea of the general trend of the patterns' frequency dependence.

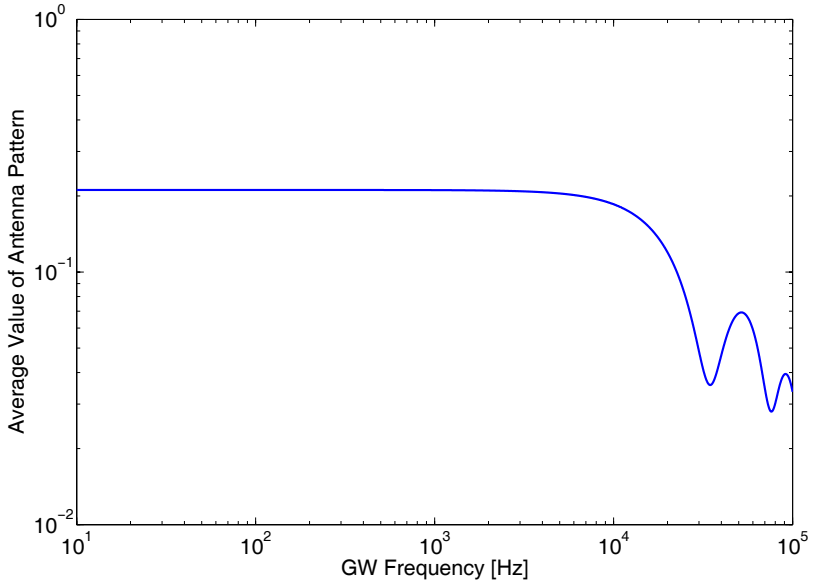

Figure 12– Average value of antenna pattern versus frequency. Patterns are averaged over all sky locations and polarizations.

From (Figure 12) we can see that at least the average of the patterns is fairly constant over the primary LIGO band and becomes more variable at higher frequencies. This fact is important for calibration at frequencies higher than the primary band. The minima correspond approximately to $f_{gw} = \frac{c}{2L} \equiv \frac{1}{2T}$ and its integer multiples. As mentioned above these frequencies are conducive to strain cancellation which decreases the average size of the antenna pattern there.

Another way to visualize the frequency-dependence of the antenna patterns is by overlaying patterns of different successive frequencies. In three dimensions the result is more confusing than useful so this is done via two-dimensional 'slices' at a constant θ or φ:

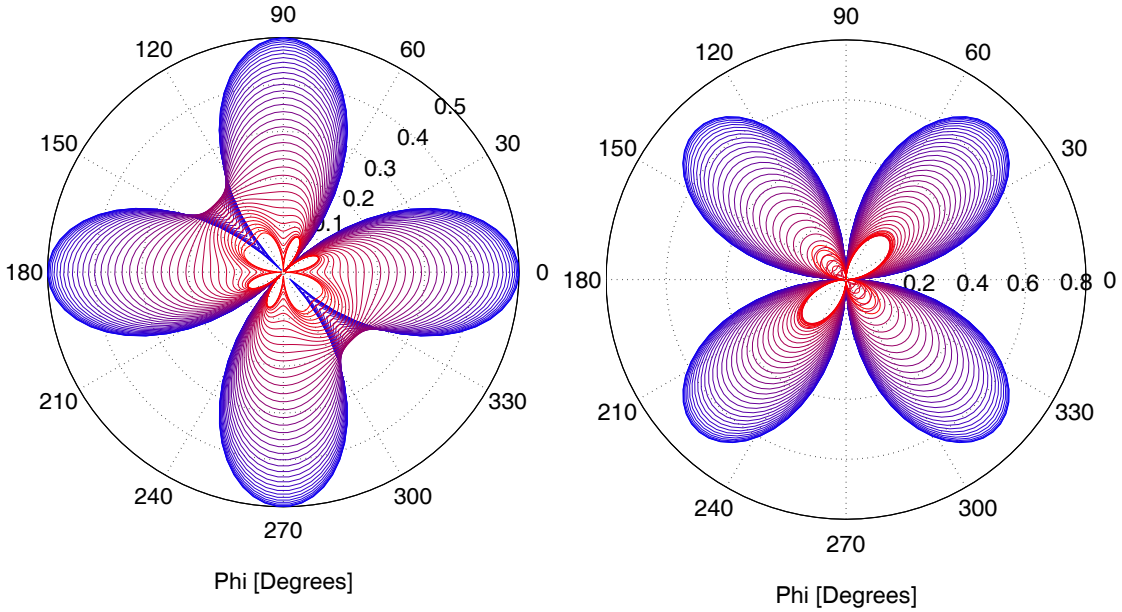

Figure 13– Overlay of antenna pattern slices at constant θ for plus (left plot, θ = 90°) and cross (right plot, θ = 45°) polarizations. The 40 slices range from DC which is pure blue to $f_{gw} = \frac{c}{2L}$ which is pure red.

Viewing the plus polarized plot in Figure 13 allows us to confirm our conclusions about the source location depicted in Figure 10. We can see that at φ = 135° the DC slice touches the origin meaning there is zero sensitivity in that direction. As frequency increases the overall size of the pattern decreases as predicted by Figure 12. However for φ = 135° there is no longer a null in the pattern. In fact at $f_{gw} = \frac{c}{2L}$ it is among the highest sensitivities.

As stated previously the current calibration procedure assumes that the detector's antenna pattern is independent of source frequency: The patterns are calculated at DC and used for all frequencies. Yet comparing the antenna patterns for plus polarized gravitational waves at DC and at f_{FSR} (Figure 8 vs. Figure 11) reveals that this assumption does not hold at high frequencies. More quantitatively one can measure a pattern's deviation from the DC pattern in the following manner. First the absolute difference is found between the DC pattern and the pattern to be compared at various angles distributed isotropicaly across the sky. Specifically for the plot shown (Figure 14) the absolute difference was found at 30 values of θ and 60 values of φ. These absolute differences are then averaged, divided by the average value of the antenna pattern at DC and at the frequency to be compared and finally multiplied by 100 to obtain a percent deviation. In addition the maximum difference is plotted as a worst-case-scenario. The two patterns to be compared are *not* scaled by the length response so the deviations measured are due strictly to the antenna pattern's frequency dependence and not the frequency dependence of the length response.

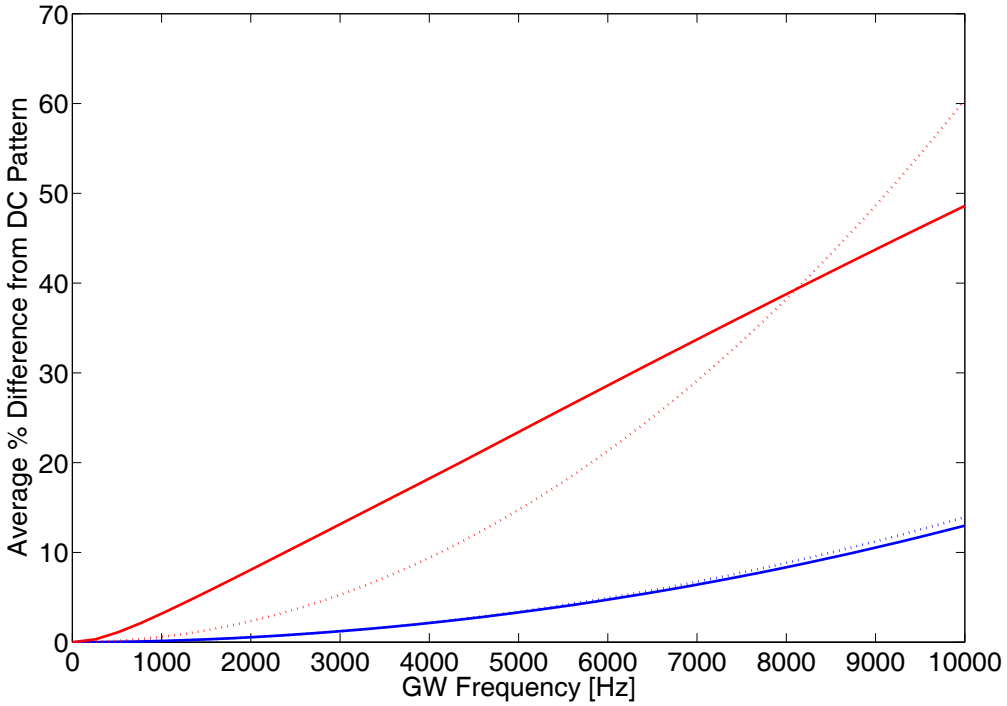

Figure 14– Antenna pattern % deviation from DC vs. frequency. Blue lines are average deviation while red lines are maximum. Solid lines are for plus polarization and dashed are for cross.

This shows that the pattern is relatively static at low frequencies, varying by less than 8% below 8 kHz, confirming that the approximation currently in place is justified. However as frequency increases the patterns alter more quickly, reaching a deviation of 12% by 10kHz. Of course any particular source could have an error much higher than this; the maximum deviation is over 30% at the upper end of the primary LIGO band. The practical meaning of this is that in the worst-case scenario the ability of the detector to sense a certain simulated source could be exaggerated by inaccurate injections, giving false hope for its real-world detection. If data collection and injection at high-frequencies is to be undertaken than the antenna patterns can no longer be assumed constant. The differences between the DC patterns and the patterns at 8 kHz can be visualized by plotting them both translucently on the same axes (Figure 15):

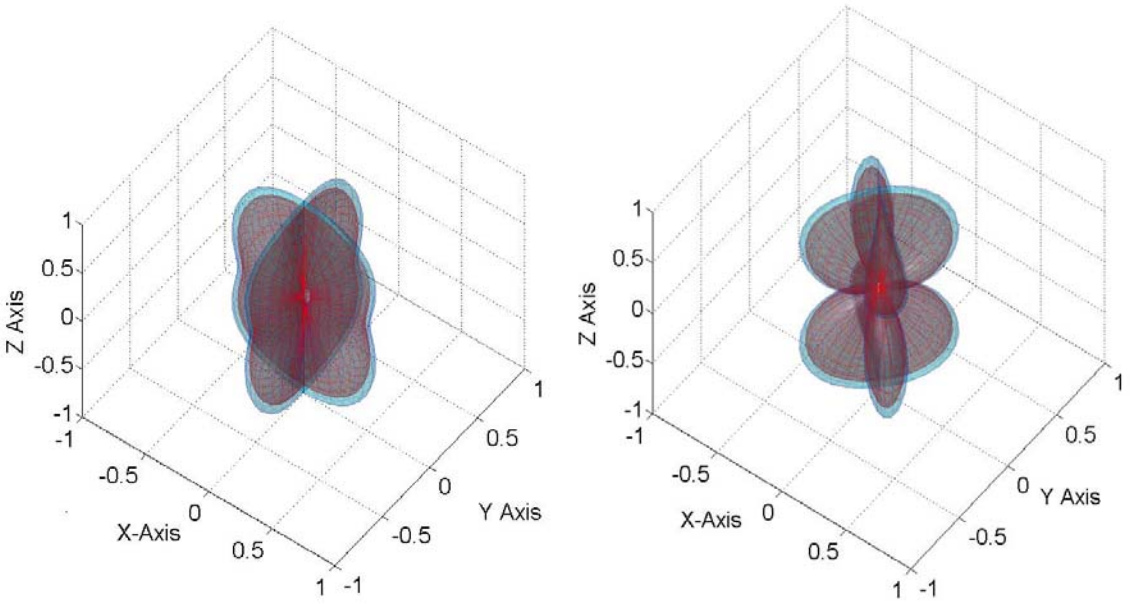

Figure 15– Comparison of antenna patterns at DC (blue) and 8 kHz (red) for plus (left) and cross (right) polarizations.

This comparison agrees with Figure 12 in that the patterns are generally smaller at 8 kHz than at DC.

In the same manner as Figure 14 we can calculate the deviation of the antenna pattern geometry from the patterns at 1FSR and 2FSR. This is useful if one wishes to approximate the antenna patterns in the vicinity of the FSRs without using a fully dynamic pattern.

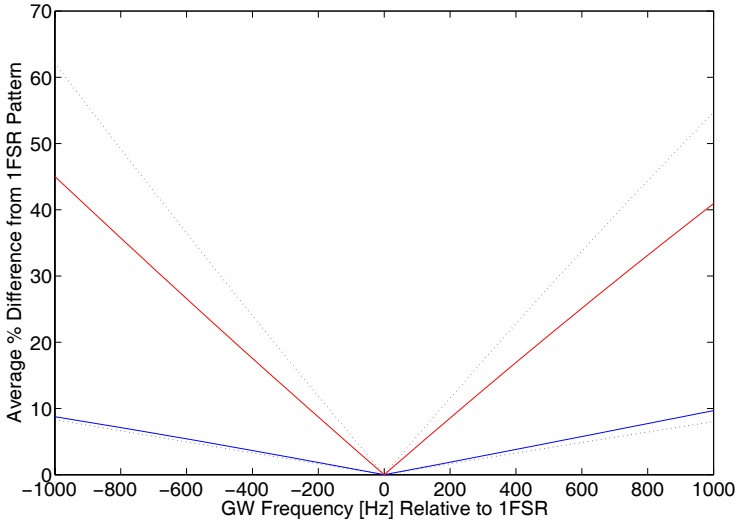

Figure 16 - Antenna pattern % deviation from 1FSR (37.52 kHz) vs. frequency. Blue lines are average deviation while red lines are maximum. Solid lines are for plus polarization and dashed are for cross.

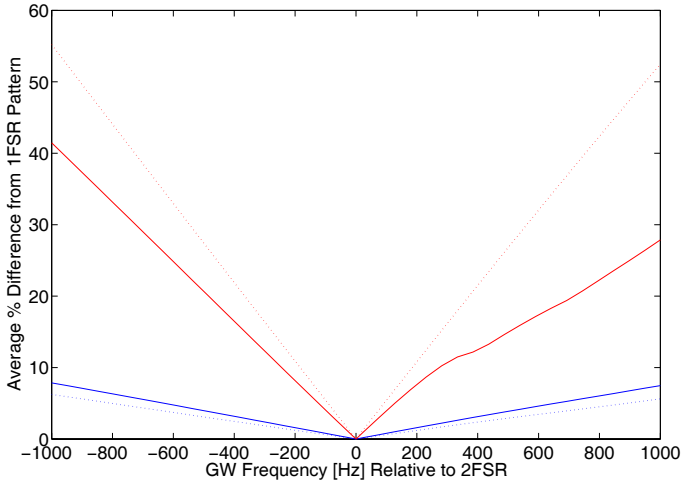

Figure 17 - Antenna pattern % deviation from 2FSR (75.04 kHz) vs. frequency. Blue lines are average deviation while red lines are maximum. Solid lines are for plus polarization and dashed are for cross.

These patterns deviate much faster than near DC; the pattern geometry at 1kHz below FSR is ~8% different from the geometry at FSR. In contrast the deviation at 1kHz away from DC was under 1%. However since the high frequency channels have a smaller bandwidth perhaps a static pattern could be assumed.

Appendix B – Length Response

The detector has a non-directional frequency dependence that arises from the filtering properties of the Fabry-Perot cavities. By filtering it is meant that the interferometer's signal responds differently to length variations of different frequencies. The magnitude of the general length to signal transfer function for a Fabry-Perot is given by[1]:

$$|H_L(f)| = \frac{1}{\sqrt{1 + F\sin^2(fT)}} \tag{2}$$

where F is the coefficient of finesse as defined in [1]. A plot of this function is shown in Figure 18.

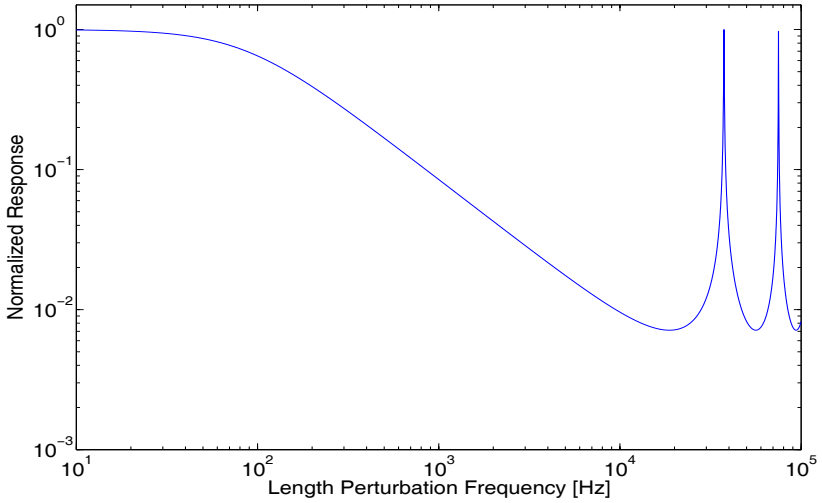

Figure 18– Cavity length response.

Additionally the full length response, including phase is given by[1]:

$$H_L(f) = \frac{1 - r_a r_b}{1 - r_a r_b e^{-i4\pi Tf}} \tag{3}$$

Where r_a and r_b are the input and end test mass reflectivity respectively.

As you can see the cavities response to length changes and similarly to GWs falls off approximately as $1/f$ for low frequencies and in general this filtering gives the detector's overall sensitivity strong frequency dependence. However this filtering effect is not a function of the source location and therefore serves only as a 'scaling factor' for the antenna pattern geometries.

As the frequency of the length variations becomes of order $1/T$ the filtering deviates from its $1/f$ behavior (Figure 18). The peaks occur where

$$f = \frac{Nc}{2L} \quad \boldsymbol{N} = 1,2,3\ldots \tag{4}$$

These frequencies bound the cavities' free spectral range and are referred to as f_{FSR}, f_{2FSR}, f_{3FSR} and so on for N=1, 2 and 3 respectively. These can be thought of as the length oscillation frequencies where from the point of view of any particular photon the length is constant. This is because although the length is changing it will return to its original position every 2T seconds (for N>1 they will return to this original position more than once every 2T but the statement still holds). Therefore to a photon that is interacting with the end test masses only every 2T seconds they appear stationary. It should be noted that by the same reasoning the cavity is resonant at $f=0$ Hz and of course the sensitivity peaks there also. In fact re-plotting Figure 18 on a linear scale reveals that the DC peak and the FSR peaks indeed have the same shape and half-width (Fig 6). For LIGO the HWHM of all of these peaks is approximately 90 Hz.

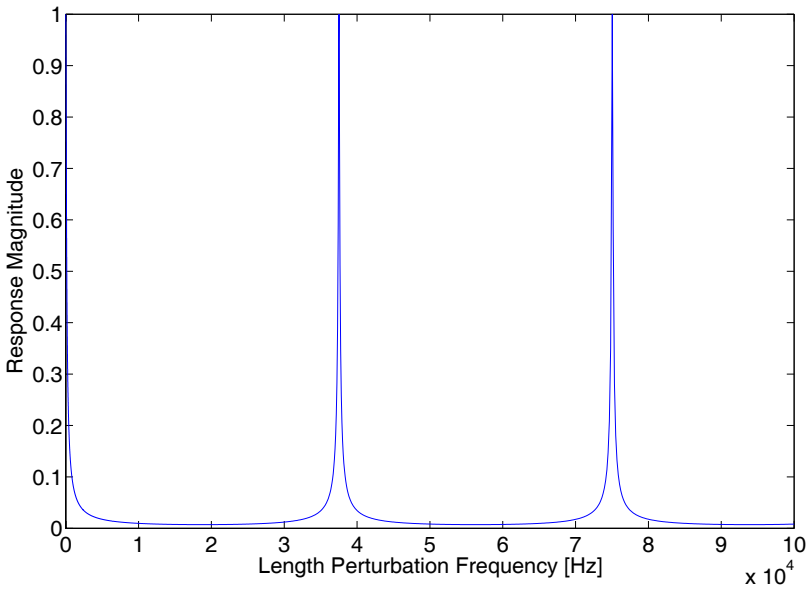

Figure 19 - Cavity length response, linear scale.

Appendix C – Overall Sensitivity

Based on the length response one might conclude that the detector's sensitivity is the same when (1) is satisfied as at DC. However this plot is for the detector's response to length changes; the overall sensitivity must include the frequency dependence of the antenna patterns such as plotted in Figure 12. A plot including both of these frequency dependencies can be produced by averaging the antenna pattern over all source sky locations and polarizations at any frequency and weighting the length response there appropriately. This is also equivalent to the product of Figure 12 and Figure 18:

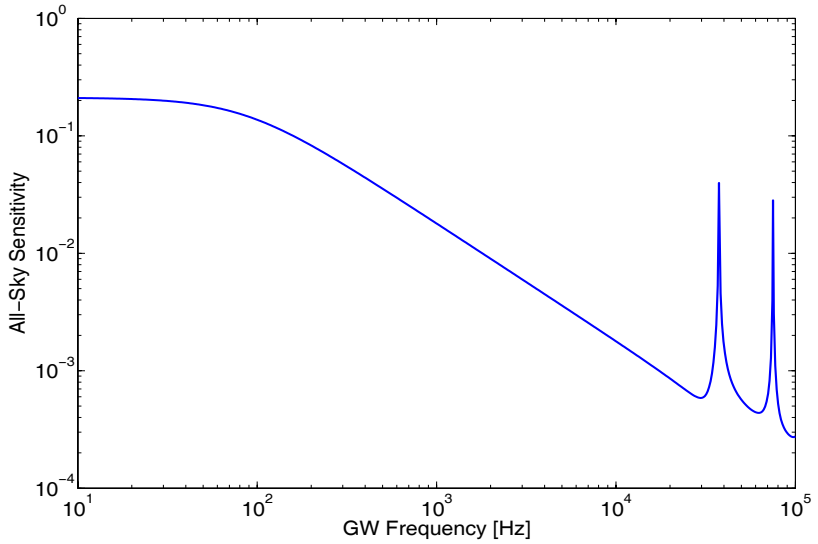

Figure 20 – Sky and polarization averaged detector response.

From Figure 20, which is proportional to the detectors overall sensitivity, we see that in actuality the sensitivity where (1) is satisfied is decreased by approximately a factor of five from its DC level. However the FSR frequencies still provide more than two orders of magnitude greater sensitivity than nearby high-frequencies i.e. 30 kHz. This property of the detector has led to proposals to search for GWs in these bands of increased sensitivity[2].

The directional sensitivity of the detector is not completely represented by either a cross or plus polarized antenna pattern. Many sources will be elliptically polarized and therefore contain both a cross and plus component. Additionally as was mentioned earlier our definition of polarization is dependent on the source location. As a result it would be helpful to view a pattern of the detector's sensitivity that is independent of polarization. These can be produced by averaging the patterns over the source orientation angle ψ which is used to define its polarization (Figure 21):

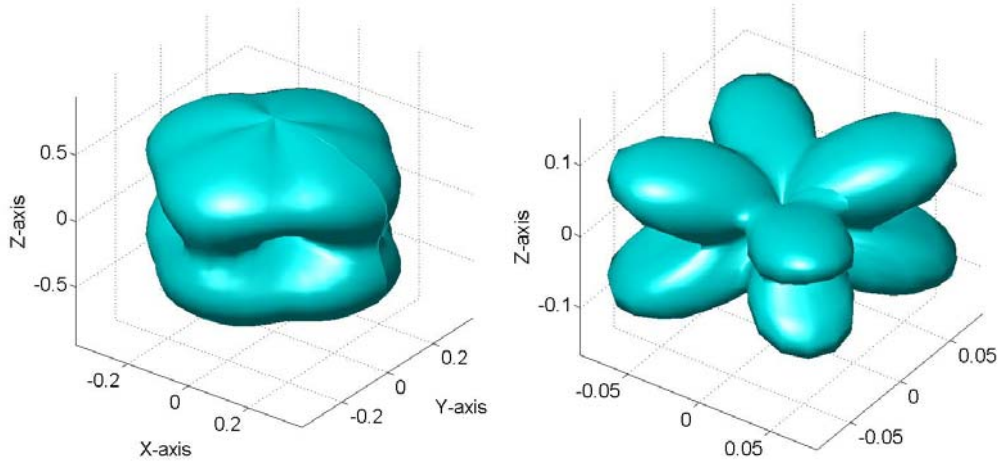

Figure 21 – Polarization-independent antenna patterns at DC (left) and $f_{gw} = \frac{c}{2L}$ (right)

Appendix D - Calibration

I. Current Procedure

The current calibration procedure is intended for low frequency gravitational waves. The low-frequency band is defined here as:[4]

$$f_{gw} << \frac{c}{2L} \tag{5}$$

Restricting oneself to this band allows the detector's response to be separated into two components. The first is a directional dependence determined as before by the geometry of the detector and the transverse nature of gravitational waves. In practice this is contained in two formulae, F_+ and F_x. These are determined from the normalized DC antenna patterns for plus and cross polarized gravitational waves respectively and assumed constant for all frequencies. The second component is a frequency dependence,

[4] For H1 $\frac{c}{2L}$ = 3.752 x 10^4 Hz.

which is determined by the filtering properties of the Fabry-Perot cavity and various noise sources and resonances. In practice this is found by driving one end test mass with a swept sine to determine the entire system's open-loop gain. This is then divided first by the actuation transfer function *A(f)*, which describes the response of the test masses to control signals of a given frequency. Next the affect of the various digital filters and the digital gain is removed. What is left is an empirical length-to-signal transfer function of the actual interferometer which is referred to as the sensing function, *C(f)*. There is of course some noise associated with this measurement and to prevent this noise from being propagated into the data during the calibration procedure it is desirable to fit the measured *C(f)* to an ideal, noise-free analytical model which can then take its place. The model to which I refer is given by equation (2). This function has an infinite number of poles given by:

$$p_n = \frac{i\pi cn}{L} - \frac{1}{\tau} \tag{3}$$

Where *n* is an integer and τ is the cavity storage time as defined in [1]. Because previously only lower frequencies were of concern *C(f)* is currently approximated, using only the 'cavity pole' at *n*=0, as:

$$H_L(f) = \frac{\omega_{cav}}{2\pi i f - \omega_{cav}} \tag{4}$$

Where ω_{cav} is p_n evaluated at *n*=0.

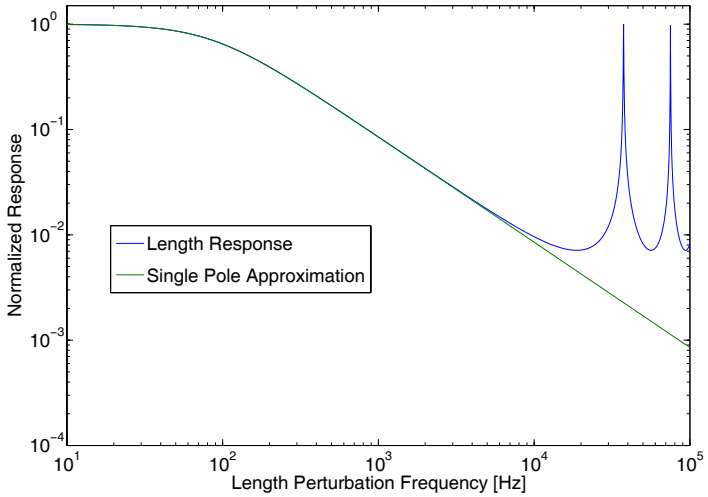

Figure 22– Comparison of full transfer function to one-pole approximation[6].

Comparing the single pole approximation that is currently used to the full transfer function (Figure 22) illustrates the limits of its application. Specifically it does not reveal the high-frequency sensitivity peaks at the FSR frequencies. If these peaks are to be used to search for high-frequency gravitational waves the calibration must account for them. Because the model currently in place defines *C(f)* strictly by its cavity pole, modifying it to the contain the first several poles or the full analytical $H_L(f)$ would be trivial.

Another aspect of calibration that becomes important upon extending the search to higher frequencies is the method for displaying and communicating calibrated sensitivities.

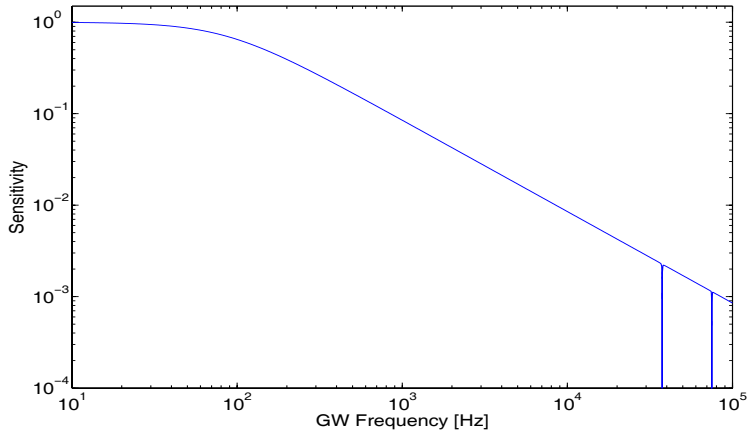

Figure 23– Conventional sensitivity plot for 'optimally-oriented' source at θ = 0° and φ = 0°.

A typical LIGO sensitivity curve is shown in Figure 23. This displays strain sensitivity vs. source frequency and avoids the complexity of the directional dependence by specifying an 'optimally-oriented' source; a plus polarized GW incident from θ and φ = 0. However comparing this plot to one for a source located at θ =90° and φ =135° reveals a problem (Figure 23 vs. Figure 24):

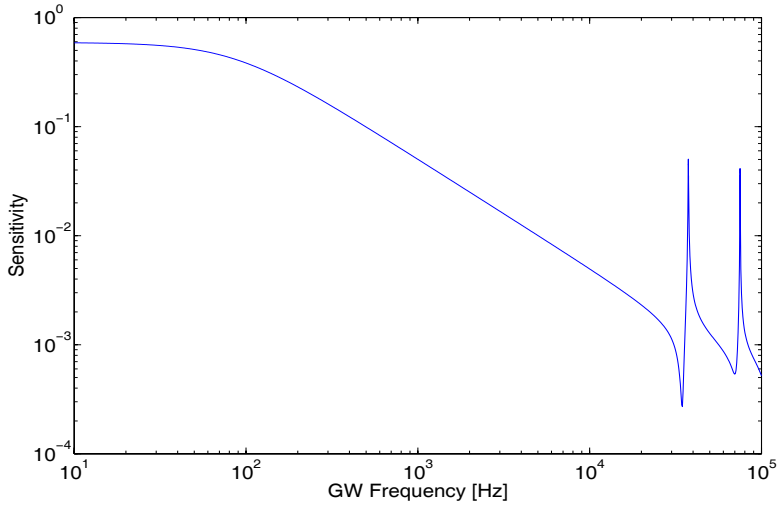

Figure 24- sensitivity plot for a source at θ =90° and φ =135°

The frequencies where $f = \frac{Nc}{2L}$ show minimums rather than maximums. Viewing a similar plot for all angles (Figure 20) reveals that this angle is not unique; the overall sensitivity of the detector peaks there. Of course the traditional plot (Figure 23) *is* correct for a source that is located at θ and φ = 0, but such a source is certainly no longer 'optimally-oriented' at higher frequencies. In short the term optimally-oriented is frequency dependent and must be treated as such. The easiest remedy would be to simply communicate sensitivities in terms of length rather than strain. Another approach would be to produce plots of the detector's Sky-Averaged response such as Figure 20. This

would still allow us to continue to give sensitivities in strain, a quantity more relevant to LIGO's goals than length sensitivity.

II. Injection

To exemplify the current process and the proposed changes let us consider a typical software injection (Figure 25).

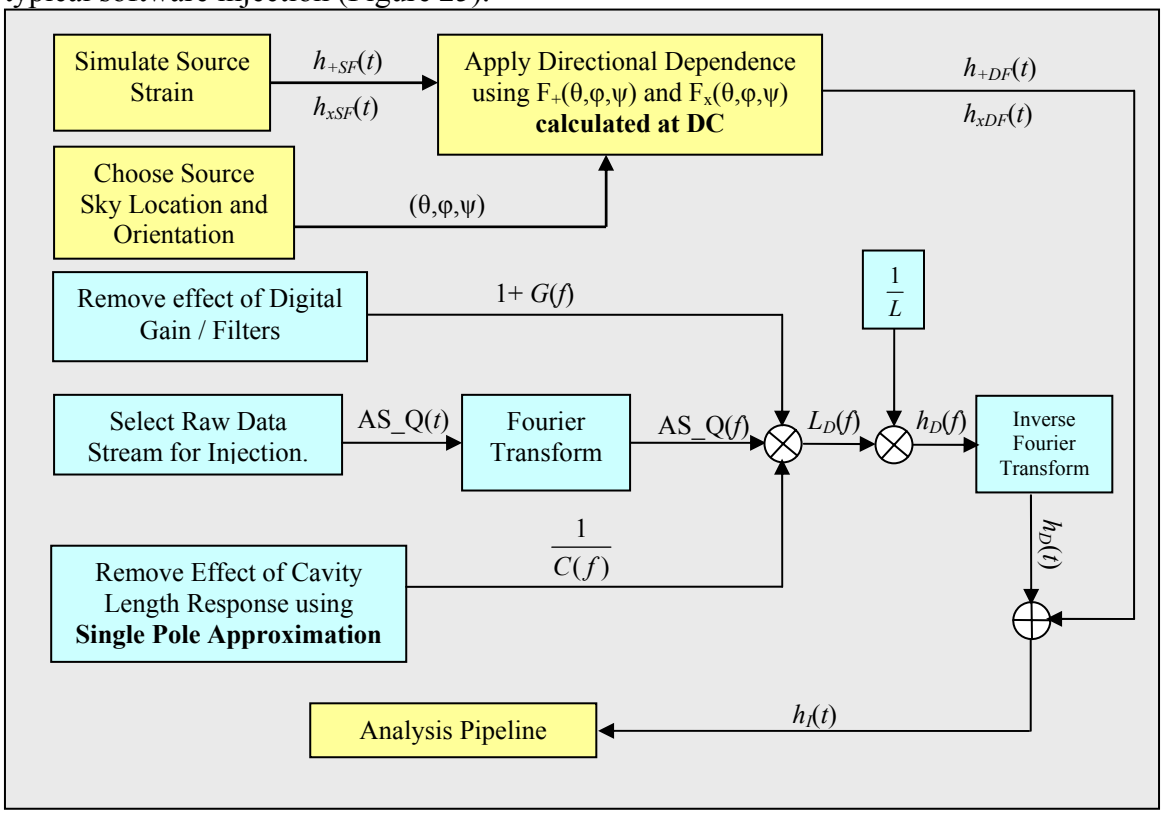

Figure 25 – Flow chart of current software injection process. Color indicates responsibility, blue being Calibration Team and yellow being injector e.g. Burst Team.

A prospective gravitational wave source e.g. a binary neutron star system is simulated giving a time series for the strain in the source frame separated into its components of each polarization, $h_{+SF}(t)$ and $h_{xSF}(t)$. The directional dependence is then taken into account giving strain in the detector frame, $h_{+DF}(t)$ and $h_{xDF}(t)$. This is done using the antenna patterns for both polarizations as calculated at DC, $F_+(\theta,\varphi,\psi)$ and $F_x(\theta,\varphi,\psi)$ *regardless of the source frequency*. The $h_{DF}(t)$ functions give the strain due to the source as would be measured in the detector. However if the simulated source were a real one this strain would be measured along with some false 'strain' due to length fluctuations caused by seismic noise, resonances and so on. Raw AS_Q data contains these noise sources but in a distorted form; the noise has been attenuated by the control system and filtered by the cavities length response. To remove the effect of the control system raw AS_Q in the frequency domain is multiplied by $1+G(f)$. This function describes the digital gain of the control system and the effect of various filters. Then the effect of the cavity's filtering is removed by multiplying by the aforementioned single pole approximation of its length response $C(f)$. Now the raw AS_Q has been converted

from the actual photodiode signal to the physical length fluctuations that the signal represents. Dividing this by L gives the strain equivalent of these length fluctuations. This 'false strain' can then be added to the source strain in the detector frame ($h_{DF}(t)$ + $h_D(t)$). The resulting noisy time series can then be run through an analysis pipeline to see if the original source strain can be recovered. This calibration technique adds systematic, frequency dependent error at two steps. The first results from the use of DC antenna patterns for all frequencies. The second stems from the use of a single pole approximation for the cavity length response.

As shown by the color-coding in Figure 25 this process is usually separated between the calibration team and whomever wishes to inject. The source is simulated and the directional dependence is accounted for by the injector. The AS_Q is converted to a calibrated time series $h_D(t)$ by the calibration team. The injector then overlays his or her simulated time series on this calibrated data. In some cases it is the injector who converts AS_Q to calibrated data but he or she does so with functions ($G(f)$, $C(f)$) provided by the calibration team.

Now a procedure is proposed which eliminates both of the aforementioned systematic errors (Figure 26).

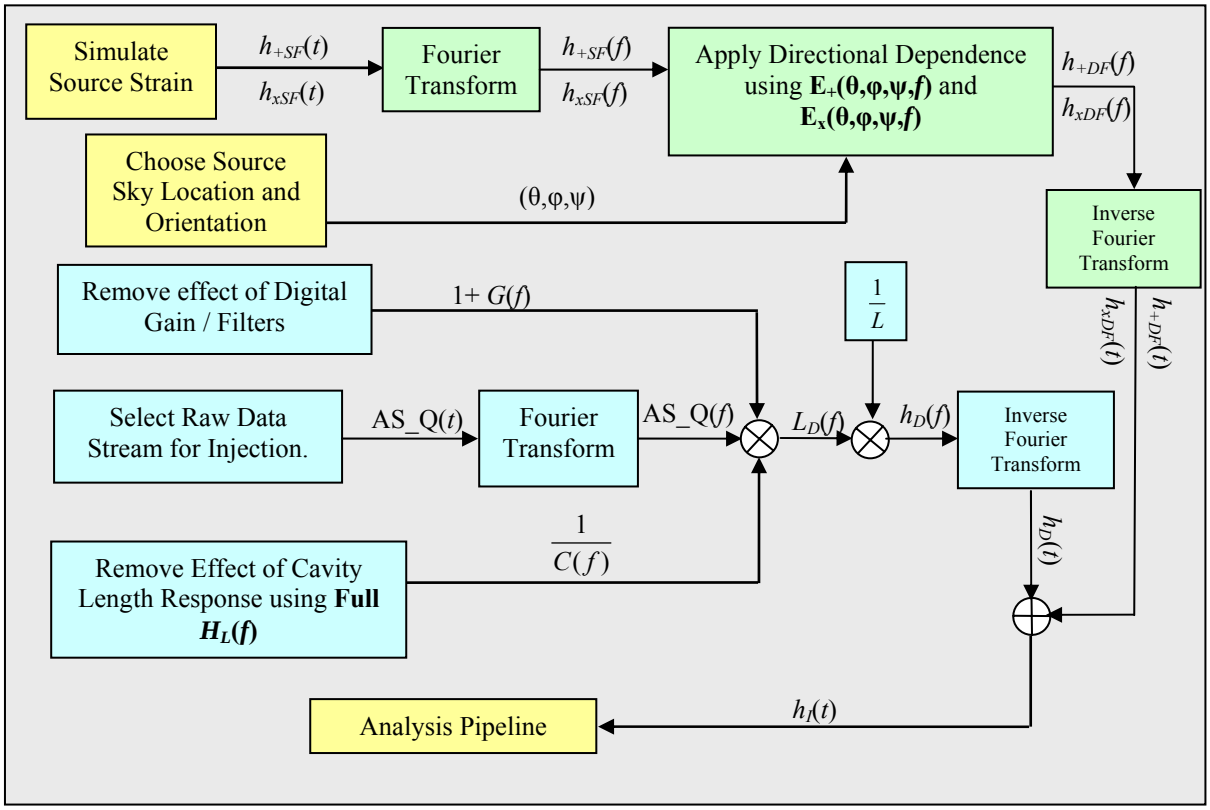

Figure 26 – Flow chart showing proposed software injection procedure. Color indicates responsibility, with blue being Calibration Team, yellow as injector and green being handled by a MatAPPS function.

Let's examine the changes. The injected signal would now no longer be scaled using the DC antenna pattern. Instead it is moved into the frequency domain where each bin can be scaled by the antenna pattern at that frequency and finally inverse-Fourier-

transformed to give a time series. The transforming and scaling would all be handled by a MatAPPS function (boxes shaded green) that accepts a time series of strain in the source frame $h_{SF}(t)$ and returns a properly scaled time series of strain as would be measured by the detector $h_{DF}(t)$. The AS_Q data is calibrated in the same manner as before with the exception that the $C(f)$ used is the full length response (5) rather than a single pole approximation. However because the mirror reflectivities are not measured during calibration but the cavity pole frequency f_{cav} is it is convenient to rewrite the length response as:

$$H_L(f) = \frac{1 - e^{-4\pi T f_{cav}}}{1 - e^{-4\pi T (f_{cav} + if)}} \tag{5}$$

Which allows the full transfer function to be defined, as the single pole approximation was before, by the cavity pole.

Thus with only minor alterations the previous division of labor can be retained. The proposed calibration procedure would allow data from the recently added high-frequency channel to be accurately calibrated. Sources could also be injected at these frequencies and finally the low-frequency calibration would no longer contain any of the systematic errors introduced by the current calibration technique.

Acknowledgements

I would like to thank my mentors Rick Savage, Greg Mendell and Malik Rakhmanov for teaching me essentially everything needed to write this paper. Rick for always being willing to take a few hours out of his day to discuss things with me, and for keeping me on track in general. Greg for teaching me more math and physics than I've ever learned in a summer and Malik for providing the Matlab code to produce the antenna patterns and the know-how that comes with writing a doctoral thesis about LIGO. I would also like to thank Mike Landry who was very helpful, patient and knowledgeable about the details of calibration. I would like to thank Terry Gunter for being my summer mom and Terry Santini for all the delicious lunches. Finally I would like to thank the NSF for the funding and Caltech for a well organized program.

References

[1] M. Rakhmanov, R.L. Savage, D.H. Reitze, D.B. Tanner, Dynamic Resonance of light in Fabry-Perot cavities, Physics Letters **A305** (2002) 239-244.

[2] D.R. Sigg, R.L. Savage, Analysis Proposal to Search for Gravitational Waves at Multiples of the LIGO Arm Cavity Free-Spectral-Range Frequency, LIGO Internal Working Note T030296-00 (2003)

[3] M. Landry, Private communication.

[4] A.C. Melissinos, M.F. Bocko, S. Giampanis, Search for a High Frequency Stochastic Background of Gravitational Waves, LSC Internal Note (2004)

[5] C. Clarkson, R. Maartens, Gravity-Wave Detectors as Probes of Extra Dimensions, Institute of Cosmology & Gravitation, University of Portsmouth (2005)

[6] M. Rakhmanov, Response of LIGO to Gravitational Waves at High Frequencies and the Vicinity of FSR, LIGO internal working note, in progress (2005)

[7] D.R. Sigg, Strain Calibration in LIGO, LIGO Technical Note T-9701011-B-D (2003)

[8] M. Rakhmanov, The Response of Test Masses to Gravitational Waves in the Coordinates of a Local Observer, Physical Review D **71**, 084003 (2005)

[9] M. Rakhmanov, Private Communication

[10] G. Gonzalez, M. Landry, B. O'Reilly, H. Radkins, Calibration of the LIGO Detectors for S2, LSC Technical Note, T040060-00-D, 2004

[11] M. Rakhmanov, F. Bondu, O. Debieu, R L Savage, Characterization of the LIGO 4 km Fabry-Perot Cavities via their High-Frequency Dynamic Responses to Length and Laser Frequency Variations, Classical and Quantum Gravity, **21,** S487-S492 (2004)

[12] R. Schilling, Angular and Frequency Response of LISA, Class. Quantum Grav. **14** (1997)